

Strain localization and fabric evolution in sand



Zhiwei Gao, Jidong Zhao*

Department of Civil and Environmental Engineering, Hong Kong University of Science and Technology, Clear Water Bay, Kowloon, Hong Kong SAR

ARTICLE INFO

Article history:

Received 20 February 2013

Received in revised form 2 May 2013

Available online 18 July 2013

Keywords:

Shear band

Anisotropy

Fabric evolution

Strain localization

Plane strain

Sand

ABSTRACT

Strain localization is frequently observed in sand and is considered an important precursor related to major geohazards such as landslides, debris flow and failure of relevant geo-structures. This paper presents a numerical study on strain localization in sand, with a special emphasis on the influence of soil fabric and its evolution on the initiation and development of shear band. In particular, a critical state sand plasticity model accounting for the effect of fabric and its evolution is used in the finite element analysis of plane strain compression tests. It is found that the initiation of shear band is controlled by the initial fabric, while the development of shear band is governed by two competing physical mechanisms, namely, the structural constraint and the evolution of fabric. The evolution of fabric generally makes the sand response more coaxial with the applied load, while the structural constraint induced by the sample ends leads to more inhomogeneous deformation within the sand sample when the initial fabric is non-coaxial with the applied stress. In the case of smooth boundary condition, structural constraint dominates over the fabric evolution and leads to the formation of a single shear band. When the boundary condition is rough, the structural constraint may play a comparable role with fabric evolution, which leads to symmetric cross-shape shear bands. If the fabric is prohibited from evolving in the latter case, a cross-shape shear band pattern is found with the one initiated first by the structural constraint dominating over the second one. In all cases, significantly larger dilation and fabric evolution are observed inside the shear band than outside. The simulated shear band orientation coincides with the Roscoe's angle for cases with high confining pressure and lies in between the Roscoe's angle and Arthur's angle for the low confining pressure cases.

© 2013 Elsevier Ltd. All rights reserved.

1. Introduction

Strain localization is frequently observed in sand and is considered an important precursor of the failure of soil and relevant geo-structures including major geohazards such as landslides and debris flow. Due to its apparent importance, relevant studies on strain localization, both experimentally and theoretically, have been an active area in geomechanics for decades (see, e.g., Chu et al., 1996; Vardoulakis, 1996; Mokni and Desrues, 1998; Desrues and Viggiani, 2004; Rechenmacher, 2006; Daouadji et al., 2011). These studies identified the following key factors which influence the strain localization in sand, including the density of sand, confining pressure, boundary conditions, sample size, imperfection and the drainage conditions. However, relatively less attention has been paid to the correlation of strain localization with the presence of fabric and its evolution in sand. The fabric in sand, or the so-call internal structure of sand attributable to the sand particle orientation, contact normal distribution and void space distribution, has been widely regarded to affect the key behavior of sand including dilatancy, liquefaction and critical state, and may

influence the behavior of strain localization in sand in an important manner as well. Indeed, based on plain strain compression tests, Tatsuoka et al. (1990) found that the shear band development was indeed dependent on the initial bedding plane orientation, or the fabric, of the sample. In their torsional shear tests, the horizontal bedding plane in the sand deposit was also shown to act as attractor to shear band. Similar observations were further confirmed by Lade et al. (2008). A more recent numerical study by Fu and Dafalias (2011) based on discrete element method with elliptical granular particles also indicated that the development of shear band depends crucially on the initial fabric orientation.

Meanwhile, it is important to realize that the fabric in sand is not stationary and may evolve constantly over different deformation stages of sand. The change of internal structure in soil due to fabric evolution may apparently affect the initiation and development of shear band. This has indeed been proved by micromechanics-based studies including distinct element simulations (e.g., Bardet and Proubet, 1991; Oda and Iwashita, 2000; Evans and Frost, 2010; Chupin et al., 2011; Fu and Dafalias, 2011; Zhao and Guo, 2013a,b; Guo and Zhao, 2013; Zhao et al., 2013) and physical tests on photoelastic rods (Oda et al., 1982; Oda and Kazama, 1998). For example, based on plane strain compression tests on sand and biaxial compression tests on rod-like particles, Oda and Iwashita (2000) have

* Corresponding author. Tel.: +852 2358 8418; fax: +852 2358 1534.

E-mail address: jzhao@ust.hk (J. Zhao).

shown that during the strain hardening process of the tested samples, a column-like fabric structure was found growing in parallel to the major principal stress direction; this structure can then be gradually changed and be totally reconstructed in the softening process, especially inside the shear band. The 2D DEM simulations of direct shear and biaxial compression tests by Fu and Dafalias (2011) using elliptical particles demonstrate that critical states can be reached at very large local shear strain within a shear band and the critical state fabric is strongly anisotropic. Indeed, as pointed out by Li and Dafalias (2012), Zhao and Guo (2013a,b) and Guo and Zhao (2013), as an essential component in addition to void ratio and stress, fabric anisotropy has to be carefully taken into account in the characterization of critical state in sand, and the soil fabric is highly anisotropic at critical state. Meanwhile, since a sample can be initially isotropic, its fabric has to experience substantial change before reaching an anisotropic critical state fabric, which highlights the importance of considering fabric evolution.

Towards the investigation of strain localization in sand, it is hence crucial to properly consider the role of fabric and fabric evolution. This is unfortunately absent in most existing studies including those derived from classic bifurcation theory (e.g., Vardoulakis, 1980,1996; Lade, 2003; Hashiguchi and Tsutsumi, 2007; Gutierrez, 2011) and those based on finite element method (e.g., Shuttle and Smith, 1988; Anand and Gu, 2000; Tejchman and Górski, 2010). Inherent fabric anisotropy has recently been considered in a hypoplastic model by Bauer et al. (2004) and Tejchman et al. (2007) in the simulation of shear band development in sand. While their studies realistically capture the dependence of shear band thickness and inclination on the initial bedding plane orientation of the sand sample, the interplay between fabric evolution and the development of shear band as two distinctive physical processes has not been properly considered. This issue will be carefully addressed in this paper. In this study, an anisotropic sand model newly developed by the authors (Gao et al., 2013) will be employed in conjunction with finite element method to investigate the strain localization in sand under plane strain compression. With a fabric evolution law embedded in this model, the effect of fabric and its evolution on the development of shear band in sand will be particularly highlighted. Based on detailed comparison between the numerical simulations and laboratory observations, the study offers further insights into the micromechanical basis of dilatancy and fabric evolution in shear bands. An interesting explanation of competing mechanisms between fabric evolution and structural constraint in the shear band development of sand under plane strain compression is also provided.

2. A critical state sand model accounting for fabric evolution

2.1. Model formulation

The model is developed based on the anisotropic critical state theory proposed recently by Li and Dafalias (2012). Detailed formulation, calibration and verification of the model at element test level can be found in Gao et al. (2013). The model features the following salient ingredients: (a) the employment of a void-based void fabric tensor which is more appropriate for describing the micromechanical basis of sand dilatancy than other fabric tensors (Li and Li, 2009); (b) accounting for fabric evolution and its effect on sand response; (c) capable of characterizing the non-coaxial sand behavior in a natural manner due to the consideration of fabric anisotropy and its evolution. Specifically, the sand model employs a yield function explicitly including the fabric anisotropy as follows

$$f = \frac{R}{g(\theta)} - He^{-k_h(A-1)^2} = 0 \quad (1)$$

where $R = \sqrt{3/2}r_{ij}$ with $r_{ij} = (\sigma_{ij} - p\delta_{ij})/p = s_{ij}/p$ being the stress ratio tensor, in which σ_{ij} is the stress tensor, $p = \sigma_{ii}/3$ is the mean normal stress, δ_{ij} is the Kronecker delta and s_{ij} is the deviator stress; H is a hardening parameter; k_h is a non-negative model constant and $g(\theta)$ is an interpolation function based on the Lode angle θ of r_{ij} or s_{ij} as follows

$$g(\theta) = \frac{\sqrt{(1+c^2)^2 + 4c(1-c^2)\sin 3\theta} - (1+c^2)}{2(1-c)\sin 3\theta} \quad (2)$$

where $c = M_e/M_c$, the ratio between the critical state stress ratio R in triaxial extension M_e and that in triaxial compression M_c .

An important inclusion in the yield function in Eq. (1) is a fabric anisotropy variable A defined by the following joint invariant of the deviatoric void-based fabric tensor F_{ij} (Li and Li, 2009) and the loading direction tensor n_{ij} (Li and Dafalias, 2012; Dafalias et al., 2004)

$$A = F_{ij}n_{ij} \quad (3)$$

where F_{ij} is a symmetric traceless tensor whose norm $F = \sqrt{F_{ij}F_{ij}}$ is referred to as the degree of fabric anisotropy. For convenience, F_{ij} is normalized such that at the critical state, F is unity. For an initially cross-anisotropic sample with the isotropic plane being the x - z plane and the deposition direction aligning with the y -axis (e.g., Fig. 3(a) with the bedding plane orientation $\alpha = 0^\circ$), F_{ij} can be expressed as below

$$F_{ij} = \begin{pmatrix} F_{yy} & 0 & 0 \\ 0 & F_{xx} & 0 \\ 0 & 0 & F_{zz} \end{pmatrix} = \sqrt{\frac{2}{3}} \begin{pmatrix} F_0 & 0 & 0 \\ 0 & -F_0/2 & 0 \\ 0 & 0 & -F_0/2 \end{pmatrix} \quad (4)$$

where $F_0 (\geq 0)$ is the initial degree of anisotropy. If the initial bedding plane orientation does not align with the coordinate system (e.g., $\alpha \neq 0^\circ$ in Fig. 3(a)), the initial fabric tensor F_{ij} can be obtained by an orthogonal transformation of Eq. (4). Note that the fabric tensor will be manipulated directly in the sequel rather than dealing with the bedding plane angle and F_0 separately. The deviatoric unit loading direction tensor n_{ij} in Eq. (3) is defined as follows (Li and Dafalias, 2004)

$$n_{ij} = \frac{N_{ij} - N_{kk}\delta_{ij}/3}{|N_{ij} - N_{kk}\delta_{ij}/3|} \quad \text{with } N_{ij} = \frac{\partial \tilde{f}}{\partial r_{ij}} \quad (5)$$

where $\tilde{f} = R/g(\theta)$. Obviously, $n_{ii} = 0$ and $n_{ij}n_{ij} = 1$.

The evolution laws for H and F_{ij} are expressed as below

$$dH = \langle L \rangle r_h = \langle L \rangle \frac{G(1-c_h e)}{pR} [M_c g(\theta) e^{-n\zeta} - R] \quad (6a)$$

$$G = G_0 \frac{(2.97 - e)^2}{1 + e} \sqrt{pp_a} \quad (6b)$$

$$dF_{ij} = \langle L \rangle \Theta_{ij} = \langle L \rangle k_f (n_{ij} - F_{ij}) \quad (7)$$

where $\langle \cdot \rangle$ denote the Macauley brackets with $\langle x \rangle = x$ for $x > 0$ and $\langle x \rangle = 0$ for $x \leq 0$; L is the loading index; e is the void ratio; c_h , n , G_0 and k_f are non-negative model parameters; G is the elastic shear modulus; $p_a (=101 \text{ kPa})$ is the atmospheric pressure; ζ is the dilatancy state parameter defined as follows (Li and Dafalias, 2012)

$$\zeta = \psi - e_A(A - 1) \quad (8)$$

where e_A is a model parameter; $\psi = e - e_c$ is the state parameter defined by Been and Jefferies (1985) with e_c being the critical state void ratio corresponding to the current mean normal stress p . In the present work, the critical state line in the e - p plane is given by (Li and Wang, 1998)

$$e_c = e_\Gamma - \lambda_c(p/p_a)^\xi \quad (9)$$

where e_r , λ_c and ξ are material constants.

Based on the yield function in Eq. (1), an associated non-coaxial flow rule in the deviatoric plane is used in the model

$$de_{ij}^p = \langle L \rangle m_{ij}, \quad \text{with } m_{ij} = \frac{\partial f / \partial r_{ij} - (\partial f / \partial r_{mn}) \delta_{mn} \delta_{ij} / 3}{|\partial f / \partial r_{ij} - (\partial f / \partial r_{mn}) \delta_{mn} \delta_{ij} / 3|} \quad (10)$$

where de_{ij}^p is the plastic deviatoric strain increment and the expression for $\partial f / \partial r_{ij}$ can be decomposed into two parts as below (see Gao et al., 2013)

$$\frac{\partial f}{\partial r_{ij}} = N_{ij} + \underbrace{\frac{\partial f}{\partial A} F_{kl} \frac{\partial n_{kl}}{\partial r_{ij}}}_{X_{ij}} \quad (11)$$

where

$$\frac{\partial f}{\partial A} = 2k_h H(A-1)e^{-k_h(A-1)^2} \quad (12)$$

The first part N_{ij} [defined in Eq. (5)] is obviously coaxial with the direction of the stress ratio tensor r_{ij} , or equivalently the direction of the stress σ_{ij} itself; and the second part X_{ij} involves F_{kl} which is attributed to fabric anisotropy and is in general non-coaxial with r_{ij} . As the sample is sheared, F_{ij} gradually evolves towards the loading direction n_{ij} (Eq. (7)), making the non-coaxial component of the deviatoric strain increment smaller and smaller. Eventually, when critical state is approached at very large strain level, F_{ij} becomes identical to n_{ij} , resulting in $A = 1$ and $\frac{\partial f}{\partial A} = 0$. Consequently, the predicted sand response is coaxial as X_{ij} vanishes.

The following fabric-dependent dilatancy relation is used in the model (c.f., Li and Dafalias, 2000, 2012):

$$D = \frac{de_v^p}{|de_q^p|} = \frac{de_{ij}^p}{\sqrt{2de_{ij}^p de_{ij}^p} / 3} = \frac{d_1}{M_c g(\theta)} \left[1 + \frac{R}{M_c g(\theta)} \right] [M_c g(\theta) e^{m\zeta} - R] \quad (13)$$

where d_1 and m are two model constants; de_v^p and de_q^p denote the plastic volumetric and shear strain increment, respectively. According to Eqs. (10) and (13), one can get the total plastic strain increment de_{ij}^p as below

$$de_{ij}^p = de_{ij}^v + de_{ij}^p \delta_{ij} / 3 = \langle L \rangle m_{ij} + \langle L \rangle D \sqrt{2/3 m_{kl} m_{kl}} \delta_{ij} / 3 = \langle L \rangle \underbrace{(m_{ij} + \sqrt{6/9D} \delta_{ij})}_{\Omega_{ij}} \quad (14)$$

An isotropic elastic stress–strain relation is used in the model,

$$d\sigma_{ij} = E_{ijkl} de_{ij}^e \quad (15)$$

where de_{ij}^e is the elastic strain increment and E_{ijkl} is the elastic stiffness matrix expressed as

$$E_{ijkl} = G(\delta_{ik} \delta_{jl} + \delta_{il} \delta_{jk}) + \left(K - \frac{2}{3} G \right) \delta_{ij} \delta_{kl} \quad (16)$$

where K is the elastic bulk modulus expressed in terms of the Poisson's ratio ν and G as the following

$$K = G \frac{2(1+\nu)}{3(1-2\nu)} \quad (17)$$

The consistency condition on the yield function [Eq. (1)] can be written as

$$df = \frac{\partial f}{\partial \sigma_{ij}} d\sigma_{ij} + \frac{\partial f}{\partial H} dH + \frac{\partial f}{\partial F_{ij}} dF_{ij} = \frac{\partial f}{\partial \sigma_{ij}} d\sigma_{ij} + \langle L \rangle \frac{\partial f}{\partial H} r_h + \langle L \rangle \frac{\partial f}{\partial F_{ij}} \Theta_{ij} = \frac{\partial f}{\partial \sigma_{ij}} d\sigma_{ij} - \langle L \rangle K_p = 0 \quad (18)$$

where K_p is the plastic modulus expressed as below

$$K_p = -\frac{\partial f}{\partial H} r_h - \frac{\partial f}{\partial F_{ij}} \Theta_{ij} = \frac{R}{g(\theta)} \left\{ \frac{G(1-c_h e)}{H} \left[\frac{Mg(\theta) \exp(-n\zeta)}{R} - 1 \right] + 2k_h k_f (1-A)^2 \right\} \quad (19)$$

Based on the additive decomposition of the total strain increment

$$d\varepsilon_{ij} = d\varepsilon_{ij}^e + d\varepsilon_{ij}^p \quad (20)$$

and the consistency equation [Eq. (17)], one has

$$df = \frac{\partial f}{\partial \sigma_{ij}} E_{ijkl} (d\varepsilon_{kl} - \langle L \rangle \Omega_{kl}) - \langle L \rangle K_p = 0 \quad (21)$$

from which the loading index is obtained as

$$L = \frac{(\partial f / \partial \sigma_{ij}) E_{ijkl}}{K_p + (\partial f / \partial \sigma_{ab}) E_{abcd} \Omega_{cd}} d\varepsilon_{kl} = \Pi_{kl} d\varepsilon_{kl} \quad (22)$$

In conjunction with Eqs. (15), (20), and (22), the following incremental constitutive relation can be obtained

$$d\sigma_{ij} = \Lambda_{ijkl} d\varepsilon_{kl} \quad (23)$$

where

$$\Lambda_{ijkl} = E_{ijkl} - h(L) (E_{ijmn} \Omega_{mn}) \Pi_{kl} \quad (24)$$

where $h(dL)$ is the Heaviside step function, with $h(dL > 0) = 1$ and $h(dL \leq 0) = 0$. Π_{kl} is defined in Eq. (22).

2.2. Calibration of model parameters

This model has been implemented in the finite element package ABAQUS through the user-material (UMAT) interface using an explicit integration method (Sloan, 1987; Sloan et al., 2001; Zhao et al., 2005a). The large strain formulation proposed by Hughes and Winget (1980) (see also ABAQUS 6.10 User Manual) was employed in the implementation. To avoid loss of focus, the detailed numerical schemes will not be provided here (see Gao, 2012). In the subsequent sections, this model will be used to investigate the behavior of strain localization for sand under plane strain compression. The test data presented by Tatsuoka et al. (1986) and Tatsuoka et al. (1990) will be employed to benchmark the model simulations. The model parameters have hence been calibrated based on the plane strain test results on Toyoura sand reported by Tatsuoka et al. (1986) which are summarized in Table 1. Note

Table 1
Model parameters for Toyoura sand.

Parameter	Symbol	Value	
Elasticity	G_0	130	
	ν	0.25	
	Critical state	M_c	1.3
		c	0.75
		e_r	0.934
λ_c		0.02	
	ξ	0.7	
Yield function	k_h	0.03	
Plastic modulus	c_h	0.8	
	n	2	
	Dilatancy	d_1	0.5
m		3.5	
e_A		0.1	
Fabric evolution	k_f	5	

that only the data prior to the peak stress ratio state were used for calibration since after which, shear band may come into effect and significantly affect the globally observed response. The initial degree of anisotropy F_0 is set to be 0.45 (which is more or less arbitrary, but it is known difficult to be calibrated as it remains a great challenge to measure the internal structure of sand with available laboratory tools). A comparison between the model predictions with test results at the material point level is shown in Fig. 1. The overall effect of fabric anisotropy on the material behavior of Toyoura sand observed in laboratory tests, including the stiffness and dilatancy, is shown to be well reproduced by the model [see Gao et al. (2013) for more material level simulations by the model]. In Fig. 1, α , ε_a , ε_v and σ_3 denote the initial bedding plane orientation with respect to the horizontal direction, the axial strain, the volumetric strain and the minor principal stress (also the confining pressure), respectively.

As already demonstrated in Gao et al. (2013), a distinct feature of the model is its capability of characterizing the non-coaxial sand behavior in a natural manner through the consideration of fabric anisotropy and its evolution. It is indeed necessary to demonstrate this feature for a soil element under plane strain compression shown in Fig. 2(a). Fig. 2(b) shows the model simulations of the non-coaxial response of sand in drained plane strain compression with three bedding plane orientations (α in Fig. 2(a)). Since isotropic elasticity is assumed in the model (Eq. (14)), the initial sand response during the elastic stage is purely coaxial (i.e., $\beta = 0$ where β , being a measure of non-coaxiality, denotes the relative angle between the major principal stress and the major principal strain directions shown in Fig. 2(a)). As the stress and the fabric are initially not coaxial with each other, the subsequent plastic strain increment will become non-coaxial with the stress (c.f., Eqs. (9)–(11)). In all three cases of bedding plane orientation, the non-coaxiality angle β reaches a peak at around $\varepsilon_1 - \varepsilon_3 = 2\%$. Beyond the peak, the overall sand response tends towards being coaxial as β

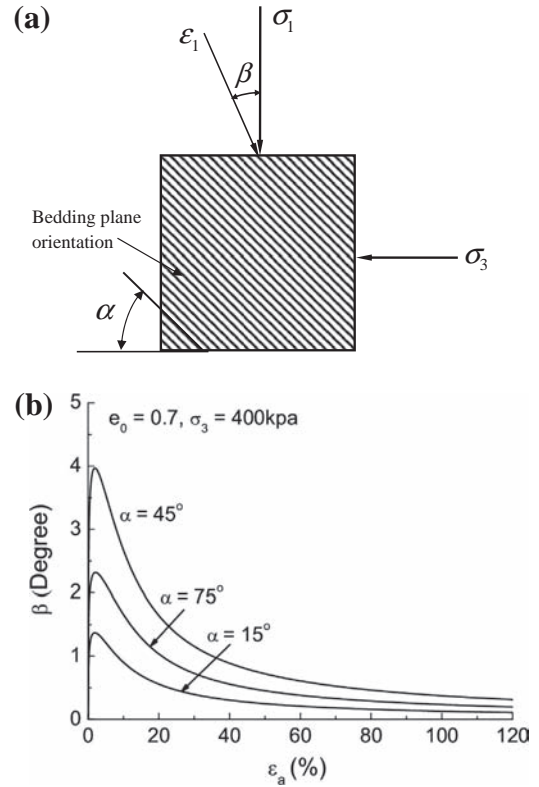


Fig. 2. (a) Definition of the bedding plane orientation α and the non-coaxiality angle β between the major principal strain direction and the major principal stress direction and (b) the model simulations of non-coaxial response for a single sand element under plane strain compression for three bedding plane orientation cases.

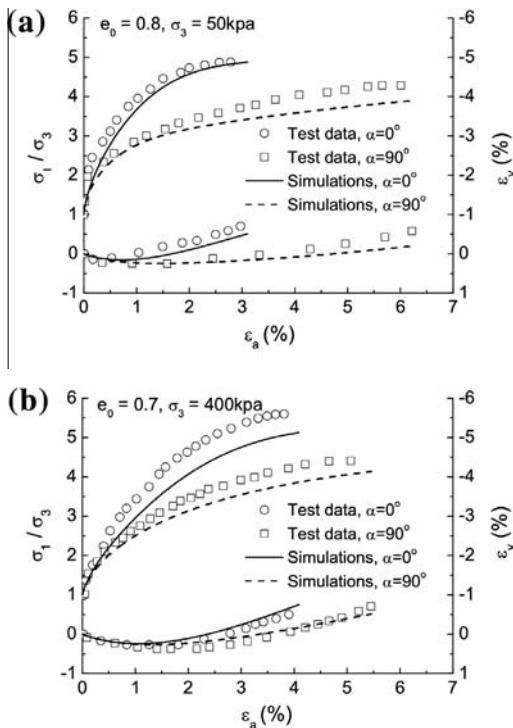


Fig. 1. Model simulations of the stress–strain response and the dilation curve of Toyoura sand in plane strain compression with (a) $e_0 = 0.8$, $\sigma_3 = 50$ kPa and (b) $e_0 = 0.7$, $\sigma_3 = 400$ kPa.

decreases, mainly owing to the evolution of fabric which results in a steady decrease of non-coaxiality (see Eqs. (10)–(12)). If the strain is adequately large (i.e., at critical state), β will totally vanish as the stress and the strain become completely coaxial. It is meanwhile found that when the bedding plane orientation has an angle of 45° with the horizontal, the non-coaxial response is the strongest with the highest peak angle β . Either increasing or decreasing the orientation angle will essentially lead to a relatively weakened non-coaxial response, as shown in Fig. 2(b) for $\alpha = 15^\circ$ and $\alpha = 75^\circ$. In addition, it is noted that when $\alpha = 0^\circ$ or $\alpha = 90^\circ$, the sand response is totally coaxial throughout the entire loading process as the fabric is initially coaxial with the applied stress and does not rotate during the entire loading process.

In the subsequent sections, the effect of fabric and its evolution on the initiation and development of strain localization in sand under plane strain compression condition will be studied numerically based on the model and its FE implementation presented above. The simulation results (shear band initiation and orientation) will also be compared with the laboratory observations presented by Tatsuoka et al. (1990). In addition, the evolution of local void ratio and fabric inside the shear band will be investigated.

3. FE analysis of strain localization in sand under plane strain compression

3.1. Setup of the plane-strain compression simulations

A series of plane-strain compression tests were conducted by Tatsuoka et al. (1990) to investigate the effect of fabric on strain localization in sand. The same plane-strain problem is chosen for the following numerical study. The sample setup, shown in

Table 2
Summary of the initial and boundary conditions for the simulated tests.

Initial void ratio e_0	Confining pressure σ_3	Boundary condition	Bedding plane orientation α
0.7	400 kPa	Rough and smooth	15°
			45°
			75°
0.7	400 kPa	Rough	0°
0.8	50 kPa	Rough and smooth	45°

Fig. 3(a) (c.f., Tatsuoka et al., 1990), is 4 cm wide and 10.5 cm high. Uniform 4-noded plane strain elements of 2.5 mm \times 2.5 mm in size are used in the finite element simulations (Fig. 3(a)). A constant confining pressure is applied in the horizontal direction of the sample, and a vertical displacement is applied to the top end of the sample by increment to ensure quasi-static loading. Two types of boundary conditions are considered in the study. The first considers smooth boundaries for both the top and the bottom ends of the sample (the bottom center is fixed to prevent rigid body movement of the sample) (Fig. 3(b)), whereas the second considers both ends are roughly constrained (Fig. 3(c)). The initial void ratio distribution is assumed to be uniform throughout the entire sample. Table 2 summarizes the initial and boundary conditions for the subsequent simulations.

3.2. Case I: smooth boundary condition

3.2.1. Non-coaxiality: the trigger of strain localization

Different measures have been used in previous FEM studies on strain localization to break the symmetry and/or homogeneity of the sample and to trigger the occurrence of strain localization, i.e., by placing imperfections in mesh or using asymmetric boundary conditions (e.g., Anand and Gu, 2000; Tejchman and Górski, 2010). More or less they are subjected to the criticisms of being arbitrary. Indeed, as a physically realistic quantity, anisotropic soil fabric can be used as a trigger for strain localization, even when everything else (i.e., material properties and the initial state) is uniform and the boundary condition is symmetric and smooth. To demonstrate this, we consider the sample with smooth boundary in Fig. 3(b) first. Upon loading, the resultant stress state for each element is close to what is shown in the element tests in Fig. 2(a) before the initiation of shear band. Due to the influence of non-coaxial fabric with respect to the stress, a non-coaxial strain field is developed in each element with its major principal direction aligning with certain angle to the left of the vertical direction. Consequently, an overall displacement field shown in Fig. 4 is developed wherein the upper part of the sample move down rightwards while the lower part to the left, which at some point triggers the strain localization in the middle part of the sample. While the occurrence of strain localization is observed for the three cases of α ($\alpha = 15^\circ, 45^\circ$ and 75°) with smooth boundary, uniform and symmetric deformation is observed when $\alpha = 0^\circ$ or $\alpha = 90^\circ$. In these

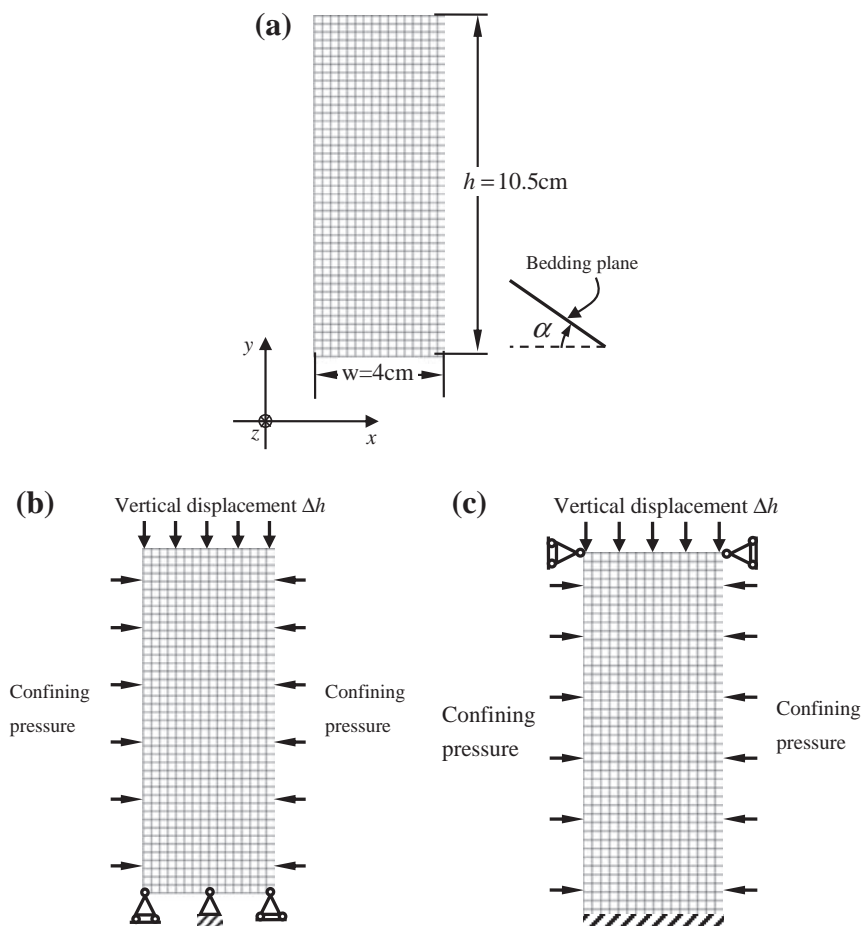


Fig. 3. (a) The sample dimension, mesh size, bedding plane orientation and the reference coordination system; schematic demonstration of (b) the smooth boundary condition and (c) the rough boundary condition for the simulations.

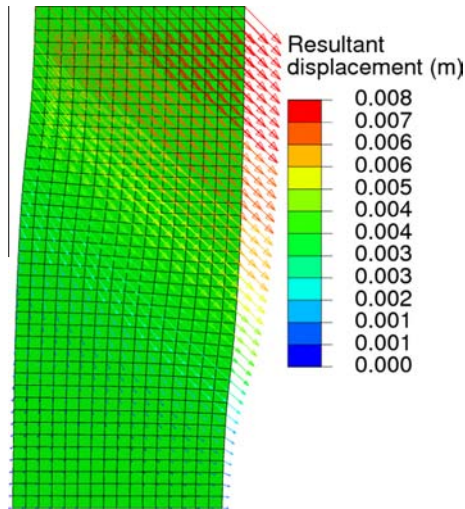


Fig. 4. Displacement field inside a sand sample with $\alpha = 45^\circ$ and smooth boundary condition ($e_0 = 0.7$, $\sigma_3 = 400$ kPa).

latter two cases, since the initial fabric is coaxial with the loading direction and the fabric does not rotate but may change magnitude during the entire loading process (see Gao et al., 2013), the response of the whole sample is predominantly coaxial ($\beta = 0$) and homogeneous, and hence no strain localization is observed. Therefore, the non-coaxial soil response caused by non-coaxial sand fabric with respect to the loading direction may facilitate the occurrence of strain localization.

3.2.2. Shear band simulation considering fabric evolution

While the initiation of strain localization is interesting, the focus of this paper is placed on the subsequent development of shear band in relation with fabric evolution and boundary conditions. We consider a sand sample shown with smooth boundary conditions shown in Fig. 3(b). Three cases of bedding plane orientation ($\alpha = 15^\circ$, 45° and $\alpha = 75^\circ$) in the sample have been considered. The global stress strain relations are shown in Fig. 5, in which σ_v denotes the global vertical stress measured at the top end of the sample, and $\epsilon_h = \Delta h/h$ is the global vertical strain, where Δh and h is the total vertical displacement and initial height of the sample, respectively. It is evident that both the initial global stiffness and peak global vertical stress decrease with α , which is consistent with the experimental observations (e.g., Tatsuoka et al., 1990). The larger α is, the later (in terms of global vertical strain) the peak appears. It is also noted that the global vertical strain level corre-

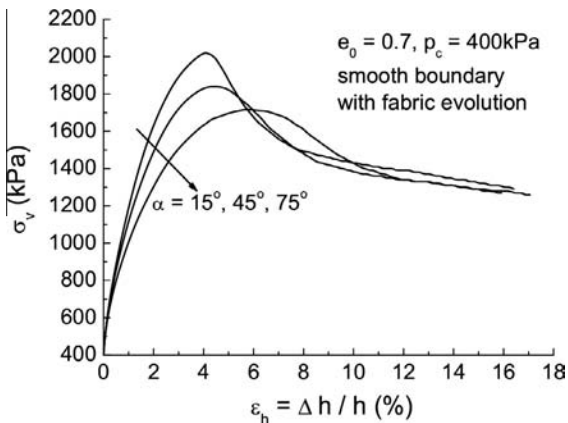


Fig. 5. Global stress–strain relations for cases with three different bedding plane orientations and smooth boundary condition ($e_0 = 0.7$, $\sigma_3 = 400$ kPa).

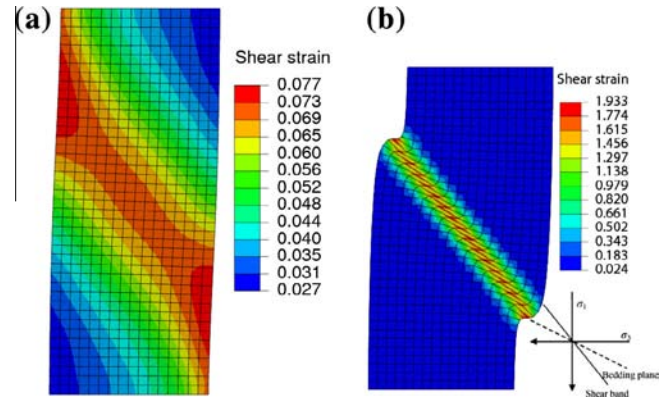


Fig. 6. Shear strain distribution for the case of $\alpha = 45^\circ$ with smooth boundary ($e_0 = 0.7$, $\sigma_3 = 400$ kPa) at (a) the peak global vertical stress state ($\Delta h/h = 4.2\%$) and (b) a post-peak stress state ($\Delta h/h = 12\%$).

sponding to the peak global vertical stress state (or the strain level for shear band initiation) increases with α from our simulations (Fig. 5), which is in agreement with the experimental data too (Tatsuoka et al., 1986,1990).

From our simulations the strain localization is found to initiate before (but close to) the peak global vertical stress. An asymmetric single band starts to develop when the global vertical stress reaches the peak (Fig. 6(a)), and becomes more concentrated at the post-peak stage (Fig. 6(b)). Fig. 6 shows the simulated shear bands for the case of $\alpha = 45^\circ$ at the peak point ($\Delta h/h = 4.2\%$)

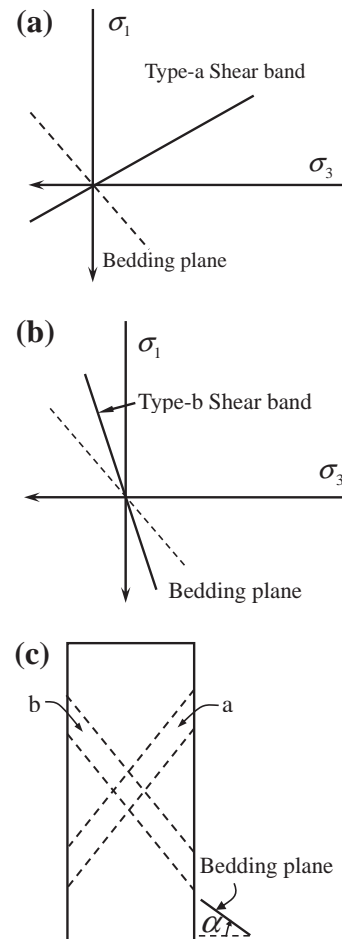


Fig. 7. (a) Type-a and (b) Type-b shear bands defined by Tatsuoka et al. (1990) and (c) their orientation inside the sample.

and at a post-peak point ($\Delta h/h = 12\%$). Such shear band development process has indeed been observed in experimental work as well (e.g., Rechenmacher, 2006), while the laboratory tests reported by Tatsuoka et al. (1986) and Tatsuoka et al. (1990) show that appreciable shear bands can be observed well before the peak stress states.

In the case of smooth boundary, shear band is found to orientate to a direction close to the zero-extension direction (Roscoe, 1970; Tatsuoka et al., 1990) and the simulated shear band orientation is close to the Roscoe's angle, which will be shown in Section 6. In addition, the simulated shear band and bedding plane are found to lie on the same side (left side in the upper part of the sample for the present study) of the major principal stress direction (see Fig. 6(b)). Tatsuoka et al. (1990) termed the similar shear band pattern they observed in laboratory tests as Type-b shear band (see Fig. 7(b)), as distinguished from a Type-a shear band pattern (Fig. 7(a)) which was also observed in their tests. Indeed, Type-b shear band is by far the most commonly observed pattern in laboratory tests with smooth boundary (Tatsuoka et al. 1990), and has also been reported in distinct element simulations (Fu and Dafalias, 2011). The formation of this pattern appears to be rather independent of the confining pressure, the initial density or the specific bedding plane orientation. Though relatively rare in the smooth boundary case, Type-a shear band has also been found in several tests by Tatsuoka et al. (1990), which is probably attributable to sample imperfection and the friction between the sample boundaries and the platen surfaces in real tests.

3.2.3. Shear band simulation considering constant fabric

To highlight the impact of fabric evolution on the shear band development, it is instructive to present a comparison case where the fabric anisotropy is fixed constant at its initial value and does not evolve at all during the loading course. This can be conveniently done by setting $k_f = 0$ in Eq. (7) with all the other model parameters being identical with the case in Section 3.2.2. Indeed, the majority of previous studies on shear band in sand considering the fabric effect have assumed a constant fabric (e.g., Bauer et al., 2004; Tejchman et al., 2007). The same three cases of bedding plane orientation with constant fabric are simulated. Fig. 8 presents the global stress–strain responses. Similar to the cases in Section 3.2.2, the initiation of shear band in the case considering constant fabric is found to occur when the global vertical stress is close to its peak (Fig. 8).

In comparison of Figs. 5 and 8, it is readily seen that fabric evolution may help a sample to achieve higher peak stress at a relatively bigger global strain level. Mathematically, this is because

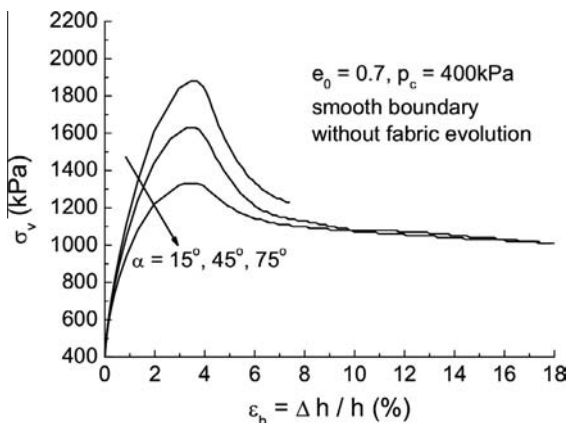


Fig. 8. Global stress–strain relations for three cases of bedding plane orientation, with smooth boundary condition and constant fabric ($e_0 = 0.7, \sigma_3 = 400$ kPa).

our model assumes the plastic shear modulus increases with the fabric evolution parameter k_f (Eq. (19)). It is physically reasonable too, since fabric evolution may help the soil to develop optimal resistance to external shear and hence may increase its strength. This is especially true when the stress and fabric are initially non-coaxial. Unlike the cases with fabric evolution shown in Fig. 5, the global vertical strain level corresponding to the peak global vertical stress state is nearly the same for all three cases of α when the fabric is assumed constant, which is inconsistent with the laboratory observations (Tatsuoka et al., 1990). In conjunction with the apparently better results in Section 3.2.2, this indicates that the fabric evolution needs to be properly considered for better simulation of strain localization in sand.

As shown in Fig. 9 for the case of $\alpha = 45^\circ$, the shear band pattern in the constant fabric case is similar to the fabric evolution case, with a Type-b single band observed. While the strain concentration at the post-peak stress state for the constant fabric case (Fig. 9(b)) is more intense than the fabric evolution case (Fig. 6(b)). It is evident that the sand adjusts its internal structure through the process of fabric evolution, which may help to alleviate the strain concentration.

3.3. Case II: rough boundary condition

By changing to rough boundary conditions as shown in Fig. 3(c), the three tests with $\alpha = 15^\circ, \alpha = 45^\circ$ and $\alpha = 75^\circ$ have been simulated again. Likewise in last subsection, the results of cases consid-

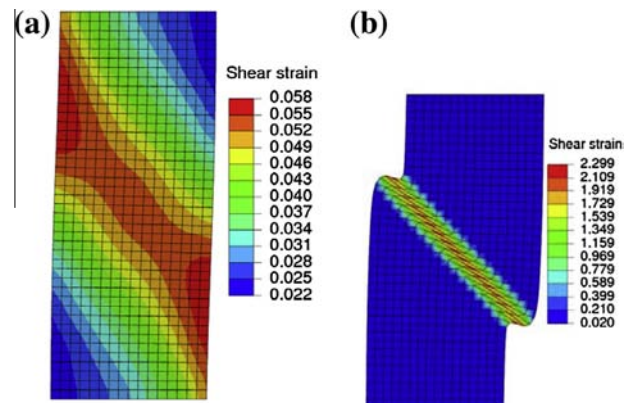


Fig. 9. Predicted strain localization for the case with $\alpha = 45^\circ$, smooth boundary condition and constant fabric ($e_0 = 0.7, \sigma_3 = 400$ kPa) at (a) the peak global vertical stress state ($\epsilon_h = 3.5\%$) and (b) a large deformation ($\epsilon_h = 12\%$).

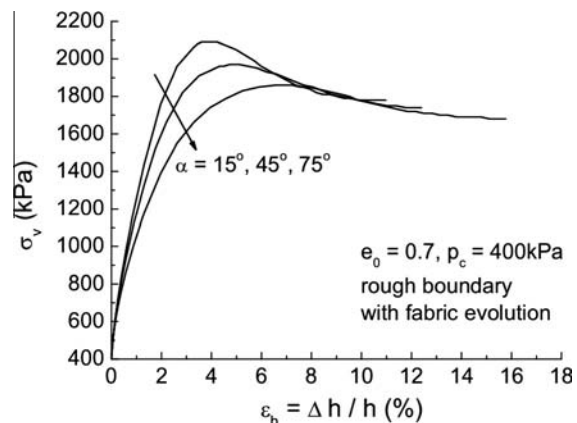


Fig. 10. Global stress–strain relations for cases with different bedding plane orientations and rough boundary condition ($e_0 = 0.7, \sigma_3 = 400$ kPa).

ering fabric evolution will be compared against the results of those with constant fabric.

3.3.1. Shear band simulation considering fabric evolution

Fig. 10 shows the global stress–strain relations for the three cases with rough boundary and fabric evolution. Similar to the smooth boundary cases presented above, both the initial global stiffness and the peak global vertical stress in the sample are found to be decreasing with α . The peak is postponed with the increase of α . The initiation of strain localization occurs before the peak global stress state. Fig. 11 shows the subsequent development of shear

band in the sample for the case $\alpha = 45^\circ$. Interestingly, with everything else identical to the case in Fig. 6 but only different boundary condition, the initiation and evolution of shear band shown in Fig. 11 are totally different from that in Fig. 6. Notably, the shear strain concentrates in the “a” direction (Fig. 7(c)) before the peak global vertical stress state (Fig. 11(a)). Evidently, this pattern shown in Fig. 11 corresponds to a Type-a shear band pattern according to Tatsuoka et al. (1990). While the orientation of this band is close to the Roccoe’s angle (which will be discussed in detail in Section 6), a further inspection indicates that it is triggered when the mobilized frictional angle for the elements inside the shear band reaches a peak value, which implies that the initiation of this shear band is governed by the Coulomb’s condition. By comparison, the inception of shear band occurs at a pre-peak mobilized friction angle for the smooth boundary case in the last subsection, which corresponds to a zero-extension failure mechanism (Tatsuoka et al., 1990).

When the global vertical strain reaches $\epsilon_h = 5.8\%$ which is beyond the peak state, shear strain concentration along direction “b” initiates and its development will gradually lead to an cross-shape double-band pattern (Fig. 11(b)), which can be seen from the strain concentration pattern at higher strain level of $\epsilon_h = 8.4\%$ and $\epsilon_h = 15.5\%$ (Fig. 11(c) and (d)). During this process, the Type-a band that occurs first is found to be dominant over the later appearing Type-b band, and the strain concentration in the former amounts to over twice as much than in the latter (Fig. 11(c)). Except the strain concentration, the two bands and deformed sample shape appear to be symmetric.

3.3.2. Shear band simulation considering constant fabric

The behavior of shear band will change significantly when the fabric is fixed for the rough boundary case. Fig. 12 shows the global stress–strain relations in the three bedding plane orientation cases. The global strain at which peak stress occurs appears to be the same for all three cases of bedding orientation, and this strain is

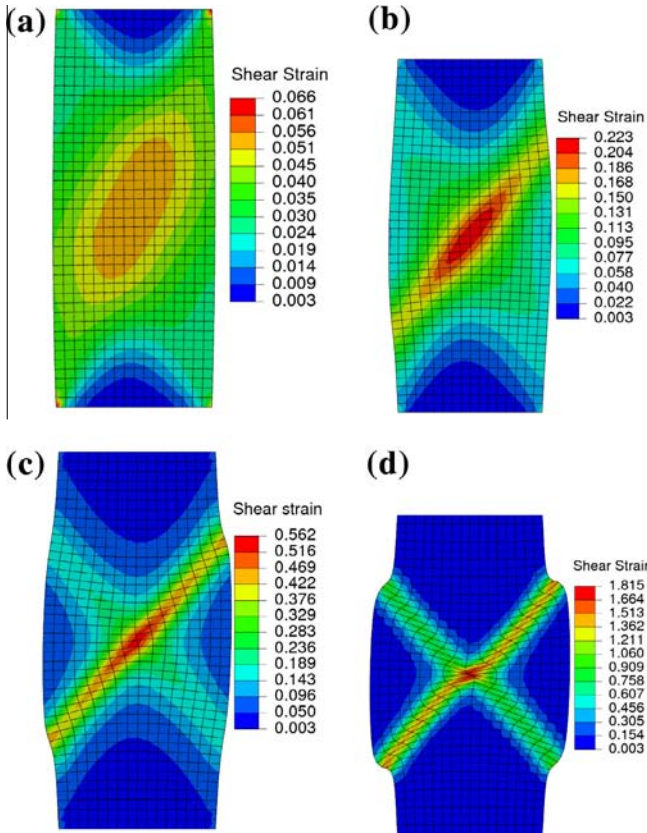


Fig. 11. Evolution of shear band for a sand sample in plane strain compression with $\alpha = 45^\circ$ ($e_0 = 0.7$, $\sigma_3 = 400$ kPa) and rough boundary at (a) $\epsilon_h = 2.8\%$ (before peak global stress state), (b) $\epsilon_h = 5.8\%$, (c) $\epsilon_h = 8.4\%$ and (d) $\epsilon_h = 15.5\%$.

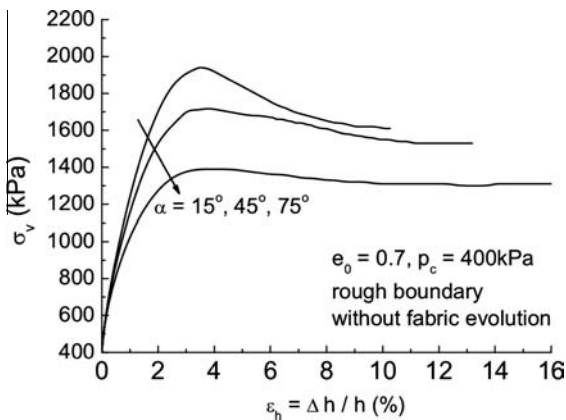


Fig. 12. Global stress–strain relations for cases with different bedding plane orientations, rough boundary condition and constant fabric ($e_0 = 0.7$, $\sigma_3 = 400$ kPa).

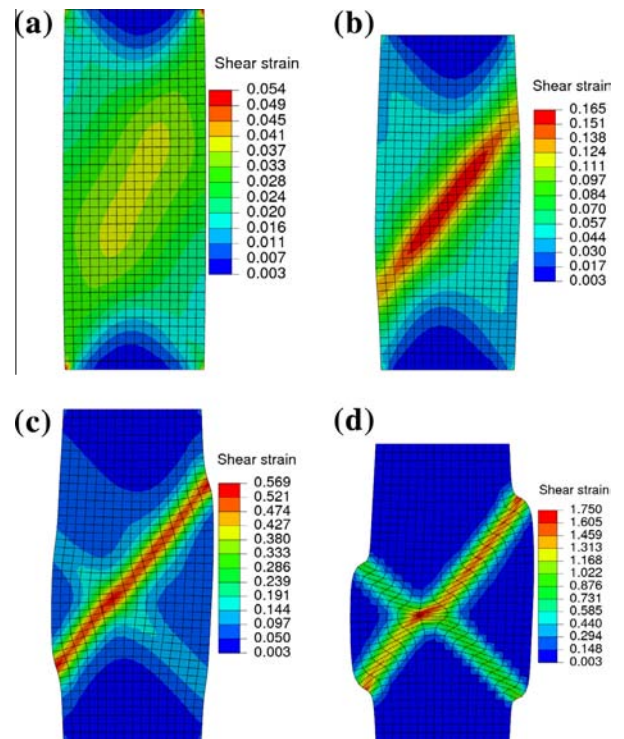


Fig. 13. Shear band development for the case with $\alpha = 45^\circ$, rough boundary condition and constant fabric ($e_0 = 0.7$, $\sigma_3 = 400$ kPa) at (a) $\epsilon_h = 2.2\%$ (before the peak global vertical stress state), (b) $\epsilon_h = 4.5\%$, (c) $\epsilon_h = 7.8\%$ and (d) $\epsilon_h = 15.6\%$.

also lower than the corresponding one in Fig. 10. The peak global stress is also significantly smaller for each case in Fig. 12 than in Fig. 10. This again confirms that fabric evolution may help the sample to develop strong peak strength in resisting the applied load. The shear band development for $\alpha = 45^\circ$ is shown in Fig. 13. The simulation results indicate that a Type-a shear band occurs first at an early loading stage which is followed by a Type-b shear band, which resembles the process observed in the case considering fabric evolution in Section 3.3.1. However, the Type-a shear band appears to be much more dominant than in the previous evolving fabric case and attracts the major localized strain in the post-peak development of the shear band. Due to the inability of self-adjusting through fabric evolution of the sample, the Type-b shear band only experiences limited development. The resultant double bands present a rather asymmetric cross-shape as shown in Fig. 13(c) and (d).

4. Mechanisms governing the shear band patterns

4.1. Competing mechanisms – structural constraint and fabric evolution

The observed differences of shear band presented in the previous section naturally provoke the following question: how does the boundary condition totally change the shear band patterns? To answer this question, it is important to understand the role of two competing physical mechanisms played in the shear band development, namely, the *fabric evolution* and the *structural constraint* imposed by the boundary conditions. The structural constraint may be better explained with the assistance of Fig. 14. In

the smooth boundary case, the top and bottom boundaries only impose normal reaction forces on the sand sample. In the rough boundary case, the sand sample is subjected to an additional pair of horizontal reaction forces (R_h) due to surface constraints at both ends. The direction of R_h shown in Fig. 10(a) is taken as being positive. Apparently, depending on the direction of R_h , there are three cases of scenario for the total reaction force R_f , as shown in Fig. 10(b)–(d), respectively.

4.1.1. Smooth boundary case

In the case of smooth boundary, there is no horizontal reaction force. So the total reaction force points vertically as in Fig. 14(c). Under the prescribed boundary condition shown in Fig. 3(b), the direction close to the bedding plane ($\alpha \neq 0^\circ$ or 90°) constitutes a natural weakened plane along which the sample can develop shear strain concentration, and the vertical reaction force will drive the upper half of the sample (Zones I + IV in Fig. 14(a)) to move down and rightwards. A single Type-b shear band is hence observed in this case. During the entire process, the structural constraint imposed by the smooth boundary and the vertical total reaction force dominate the overall development of the shear band. Fabric evolution, if considered in this process, may have attempted to adjust within the sample to reduce non-coaxial response. However, since the shear band has initiated at relatively low strain level, the influence of fabric is too late and only marginal and is indeed confined within the localization zone, which cannot compete against the structural constraint (see, e.g., Fig. 6). This can be seen from the distribution of fabric anisotropic variable A in Fig. 15(a). The effect is more obvious if the fabric is fixed as a constant (Figs. 9 and 15(b)). Due to the fabric evolution, the strain concentration in the former case (Fig. 6(b)) is slightly less intense than the latter

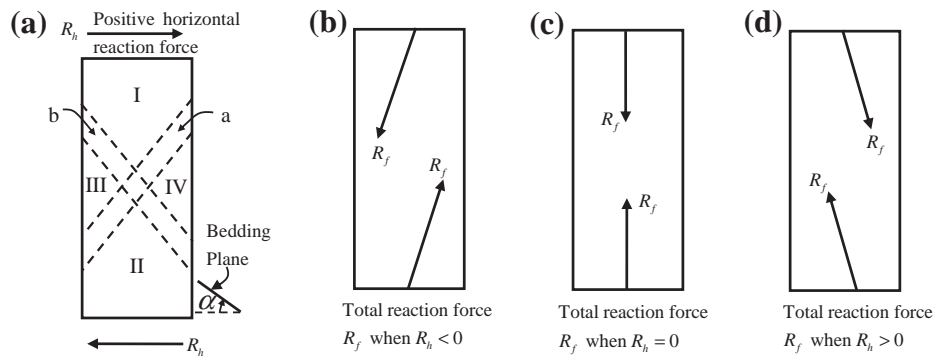


Fig. 14. Definition of (a) the positive direction of the horizontal reaction force and (b–d) three cases of the total reaction force imposed on the sample by the boundary.

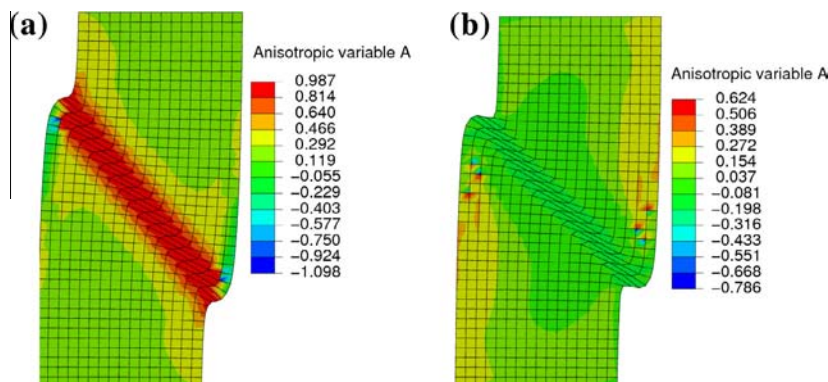


Fig. 15. Distribution of fabric anisotropic variable A [defined in Eq. (3)] at $\epsilon_h = 11\%$ for sand sample with $\alpha = 45^\circ$ and smooth boundary ($e_0 = 0.7$, $\sigma_3 = 400$ kPa): (a) considering fabric evolution; (b) constant fabric.

one (Fig. 9(b)), whereas A has more intensely evolved within the shear band in the former case (Fig. 15(a)) than in the latter case (Fig. 15(b)).

4.1.2. Rough boundary case

The $\alpha = 45^\circ$ case with rough boundary is again taken for the following discussion. We first consider the *evolving fabric* case. The change of horizontal reaction force R_h at the top surface of the sample has been monitored and is presented in Fig. 16(a). It is evident that due to the change of R_h , the total reaction force R_f changes steadily both its orientation and its magnitude in the loading process. Upon loading, due to non-coaxial sand response, the sample tends to develop a similar displacement field as shown in Fig. 4, which results in a negative horizontal reaction force R_h by the top/bottom boundaries which attempts to prevent such a trend, and hence a total reaction force R_f in the case of Fig. 14(b). When R_f rotates to the direction approximately perpendicular to the “a” direction at $\epsilon_h = 2.8\%$ (see the first downwards peak of R_h in Fig. 16(a) and Fig. 14(b)), a stress field, jointly created by R_f (in a distributed manner along the top/bottom surface) and the lateral confinement, reaches a critical condition satisfying the Roscoe’s failure condition along the “a” direction in Fig. 14(a). The homogeneity and symmetry of the material response are thus broken and strain localization initiates along direction “a” in Fig. 11(a). Note that during this process, due to the top end constraint, the sample has not experienced excessive one-way lateral movement. The existing bedding plane in this case is thus not the major trigger of localization as in the case of smooth boundary; nor does fabric evolution play a significant role in this process.

Since its inception, the Type-a band in the sample continues to develop, and thus, the shear resistance of the material in the direction “a” decreases. As a result, the magnitude of the negative horizontal reaction force R_h also changes from its negative peak

steadily to zero (shear deformation becomes less concentrated along direction “a”). Roughly the zero R_h moment ($\epsilon_h = 5.8\%$) corresponds to the instant that the Type-b shear band initiates (Figs. 11(b) and 16(a)). Due to the subsequent development of Type-b shear band, the upper part of sample (Zones I+IV in Fig. 14(a)) tends to move to the right, which induces a gradually increasing R_h in the positive direction. The resultant total reaction force R_f thus turns to become the case of Fig. 14(d). Again, such shear band development weakens the material in direction “b” continuously and R_h reaches a positive peak value at $\epsilon_h = 8.4\%$ when obvious cross shear bands are observed (Fig. 11(c)) and then decreases (Fig. 16(a)). Importantly, the occurrence of the second Type-b band does not prevent the further development of the existing Type-a band. With the overall movement of the upper body (Zone I) being mainly downwards, both bands develop steadily. Since the Type-a band occurs first, it develops an obviously more intensified band than the Type-b band.

Meanwhile, the sand fabric evolves significantly so as to lead the strong direction of the material (e.g., the perpendicular direction to the initial bedding plane, or close to direction “a”) to rotate towards the major compressive direction (vertical in this study) to increase the sample resistance to shearing. When the second shear band penetrates the sample in the horizontal direction at $\epsilon_h = 15.5\%$ (Fig. 11(d)), the evolution of fabric eventually leads to rather symmetric geometry of the two bands and sample shape (though the strain concentration is still different in the two bands). Consequently, the moving tendency of the upper sample body (Zone I shown in Fig. 14(a)) becomes totally downward without any tendency of lateral movement. At this moment, the horizontal reaction force totally vanishes and keeps constant (Fig. 16(a)), which indicates a totally vertical reaction force (Fig. 14(c)). This is due to that the fabric evolution gradually makes the sand fabric more symmetric about the vertical axis (or more coaxial with the applied stress) and facilitates the development of both symmetric shear bands and deformed sample shape (or enhances the strain concentration in Type-b shear band which appears later in these cases). A typical example for demonstrating this effect is the $\alpha = 0^\circ$ case shown in Fig. 17, in which the fabric is initially symmetric about the vertical axis and coaxial with the applied stress and symmetric cross shear bands and deformed sample shape are observed at large deformation. Apparently, while the double bands have been mainly caused by the reaction force exerted by the structural constraint, the evolution of fabric contributes importantly to form a symmetric cross-shape final pattern for this case.

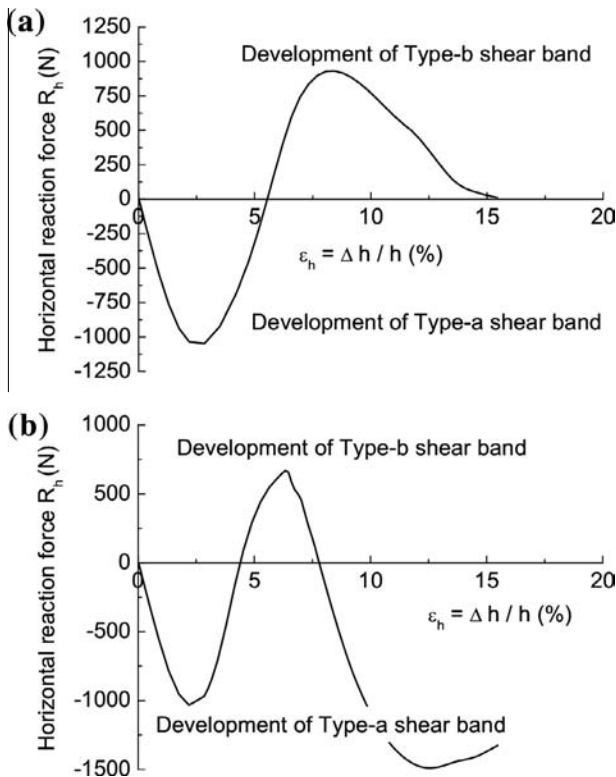


Fig. 16. Evolution of the horizontal reaction force at the top end of the sand sample with $\alpha = 45^\circ$ and rough boundary condition ($e_0 = 0.7$, $\sigma_3 = 400$ kPa): (a) considering fabric evolution; (b) considering constant fabric.

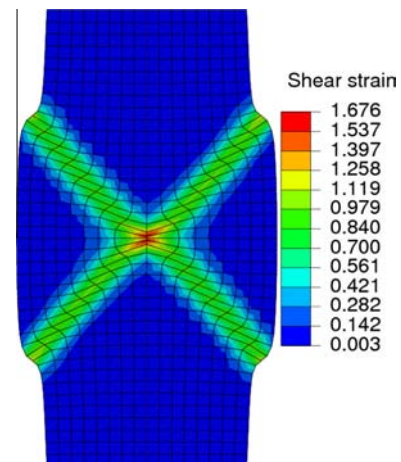


Fig. 17. Simulated shear band pattern for the case with $\alpha = 0^\circ$ and rough boundary condition at $\epsilon_h = 12\%$ ($e_0 = 0.7$, $\sigma_3 = 400$ kPa).

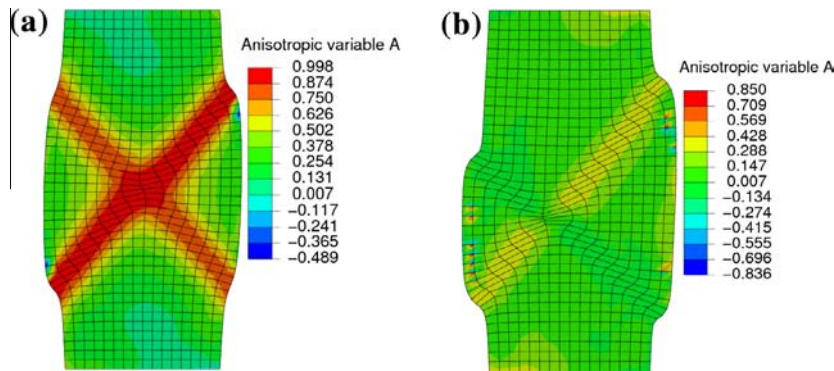


Fig. 18. Distribution of the anisotropic variable A inside the sample for the case with $\alpha = 45^\circ$ and rough boundary at $\varepsilon_h = 14\%$ ($e_0 = 0.7$, $\sigma_3 = 400$ kPa): (a) considering evolving fabric; (b) considering constant fabric.

If *constant fabric* is considered in the simulation, the initiation and development of Type-a and Type-b bands is rather similar to the above evolving fabric case until $\varepsilon_h = 7.8\%$, as indicated by the change of horizontal reaction force shown in Fig. 16(b). However, the development of Type-a shear band development continues dominating even after the Type-b shear band initiates due to the constant fabric constraint (Fig. 13(b) and (c)). When the total horizontal reaction force R_h reaches 0 for the second time at $\varepsilon_h = 7.8\%$, the strain concentration along Type-a shear band is much greater and the sample shape is asymmetric (Fig. 13(c)) (note that the deformed sample shape is nearly symmetric when R_h reaches 0 for the second time with fabric evolution). Therefore, the upper sample (Zones I + III shown in Fig. 14(a)) keeps moving along the “a” direction to the left side, which results in a steadily increasing negative R_h (Fig. 16(b)) rather than a constant one observed in the fabric evolution case at $\varepsilon_h = 15.5\%$ (Fig. 16(a)). Without fabric evolution, the sample cannot reverse this leftwards moving trend, an asymmetric cross-shape shear band pattern is hence formed at a large deformation of $\varepsilon_h = 15.6\%$ (Fig. 13(d)). Indeed, it is also evident from the observation of the anisotropic variable A shown in Fig. 18 at $\varepsilon_h = 14\%$ when both shear bands are stably formed. In the case considering evolving fabric, in both bands A reaches a value close to 1, which implies the fabric has experiences considerable rotation to try to align with the rotating principal stress direction. For the case without fabric evolution, A remains close to the initial value (about 0) in most part of the sample and around 0.3 inside the Type-a shear band. Such small change in fabric shown in Fig. 18(b) is not surprising considering that the evolution of A is purely due to the change in stress direction in this case.

5. Local material response and the micromechanical mechanisms

While the overall shear band patterns in previous sections are interesting, the local response in the material body may help to understand the material behavior from a micromechanical perspective. In particular, we extract relevant information of the state variables from the integration points of two elements shown in Fig. 19 for detailed study (Element A inside the shear band and Element B outside).

5.1. Evolution of local void ratio

Numerous experimental evidence indicates when shear band occurs, significant volumetric expansion will concentrate inside the shear band while the volumetric change is generally very small outside (see, e.g., Oda et al., 1982; Desrues et al., 1996; Oda and

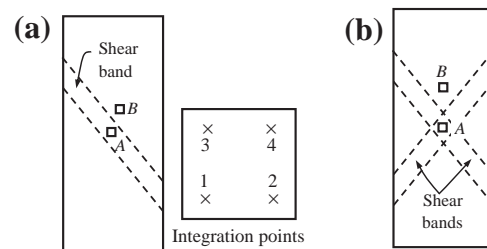


Fig. 19. Location of the selected elements and integration points for cases with (a) single shear band and (b) cross shear band.

Iwashita, 2000). Based on a 2D DEM study, Fu and Dafalias (2011) argued that, after the initiation of shear band at relatively small deformation, strain localizes in the shear band and the remaining of the sample nearly stops deforming. Our FEM simulations support these observations too, as can be seen from Fig. 20 for the case with $\alpha = 45^\circ$ and smooth boundary ($e_0 = 0.7$, $\sigma_3 = 400$ kPa). Fig. 20(a) shows the void ratio distribution at $\varepsilon_h = 11\%$ and Fig. 20(b) presents the evolution of void ratio for the two chosen elements. Notably, the void ratio for the element inside the shear band (e.g., Element A) can reach as high as 0.87 while it is around 0.75 for the element outside (e.g., Element B) which is quite close to the initial void ratio 0.7 (Fig. 20(b)). Note that the void ratio at all four integration points is found nearly identical in each of the chosen elements. Oda and Kazama (1998) indeed pointed out that the concentrated buckling of column-like structure (or the contact force chains) inside the shear band they observed from their experiments may have helped to create larger void space inside the shear band than outside.

5.2. Local fabric evolution

A distinct feature of the model used here is the consideration of fabric evolution with plastic shear deformation. Figs. 21 and 22 respectively show the simulated evolution of F and A for the two selected elements shown in Fig. 19 for the $\alpha = 45^\circ$ case with smooth boundary (data recorded for the integration point 1 of the two elements). It can be seen that F shows an initial drop at the initial loading stage. This is due to that the initial fabric and the loading direction are non-coaxial and the fabric needs to rotate towards the loading direction with plastic shear strain (see also Gao et al., 2013). Beyond a global strain level of $\Delta h/h = 4.3\%$, F gradually increases as the sample is sheared and reaches a constant value at each integration point. The fabric anisotropic variable A increases with the global strain at the initial stage and steadily approaches a constant value at both integration points. It is evident

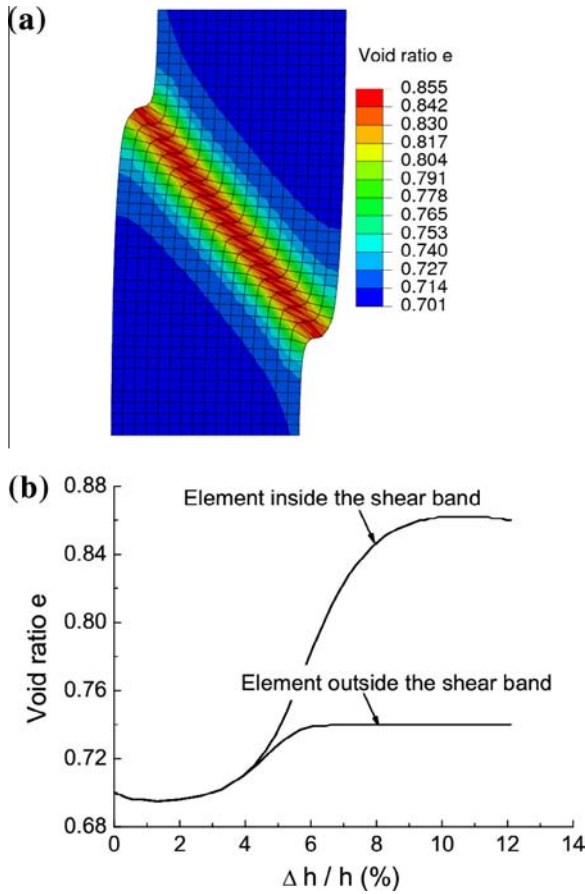


Fig. 20. (a) Void ratio distribution inside the sample ($\epsilon_h = 11\%$) and (b) the evolution of local void ratio for elements inside and outside the shear band in the case with $\alpha = 45^\circ$ and smooth boundary ($e_0 = 0.7$, $\sigma_3 = 400$ kPa).

that the final F and A is much bigger for elements inside the shear band (Figs. 21(b) and 15(a)) than those outside. This is owing to that the shear strain concentrates more within the shear band and more significant fabric evolution induced by the plastic shear strain occurs there too. Such evolutions of F and A are essentially related to the development and reconstruction of the column-like structure as observed by Oda and Kazama (1998). Note that from a micromechanical point of view, the buildup and collapse of force chains reach an equilibrium at critical state, which gives rise to steady values of macroscopically averaged variables such as stresses, void ratio, F and A .

6. The orientation of shear band

Experimental evidence indicates that the shear band orientation θ with respect to the minor principal stress direction falls normally to the bounds by two angles as follows (e.g., Vardoulakis, 1980; Oda and Iwashita, 1999)

$$\theta_R \leq \theta \leq \theta_C \quad (25)$$

where the lower bound $\theta_R = 45^\circ + \psi_{\max}/2$ is the Roscoe's angle and the upper bound $\theta_C = 45^\circ + \varphi_{\max}/2$ is the Coulomb's angle. ψ_m and φ_m respectively denote the maximum dilation angle and friction angle defined as below

$$\psi_{\max} = \arcsin \left[\frac{(d\epsilon_1/d\epsilon_3)_{\max} + 1}{(d\epsilon_1/d\epsilon_3)_{\max} - 1} \right] \quad (26)$$

$$\varphi_{\max} = \arcsin \left[\frac{(\sigma_1/\sigma_3)_{\max} - 1}{(\sigma_1/\sigma_3)_{\max} + 1} \right] \quad (27)$$

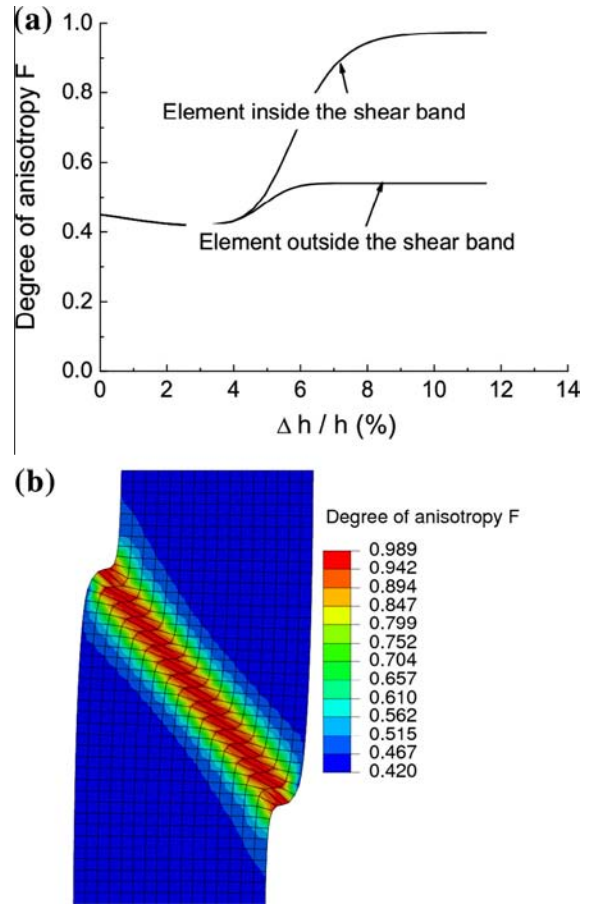


Fig. 21. (a) The local evolution of F for the elements inside and outside the shear band and (b) distribution F at $\epsilon_h = 11\%$ for the case with $\alpha = 45^\circ$ and smooth boundary ($e_0 = 0.7$, $\sigma_3 = 400$ kPa).

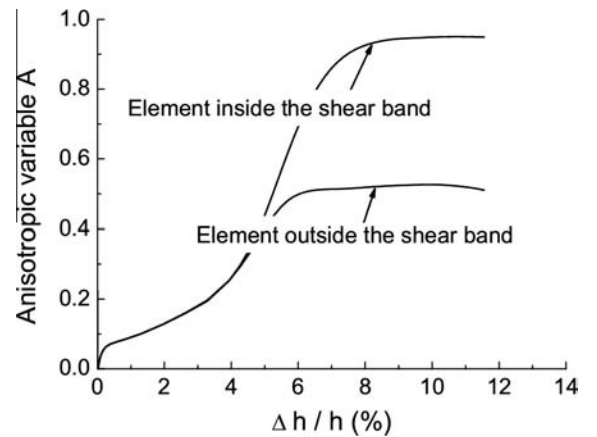


Fig. 22. The local evolution of A for the elements inside and outside the shear band for the case with $\alpha = 45^\circ$ and smooth boundary ($e_0 = 0.7$, $\sigma_3 = 400$ kPa).

where $d\epsilon_1$ and $d\epsilon_3$ denote the major and minor principal strain increments, respectively. For the plane strain compression tests considered here, the physical significance of Roscoe's angle (Roscoe, 1970) is that shear band will develop in the direction along which the tensile strain increment is zero (or the strain increment perpendicular to the shear band is zero). The Coulomb's angle essentially indicates that the shear band develops along the plane on which the maximum internal friction is mobilized. Based on experimental observations, Arthur et al. (1977) proposed that the shear band orientation $\theta = \theta_A = 45^\circ +$

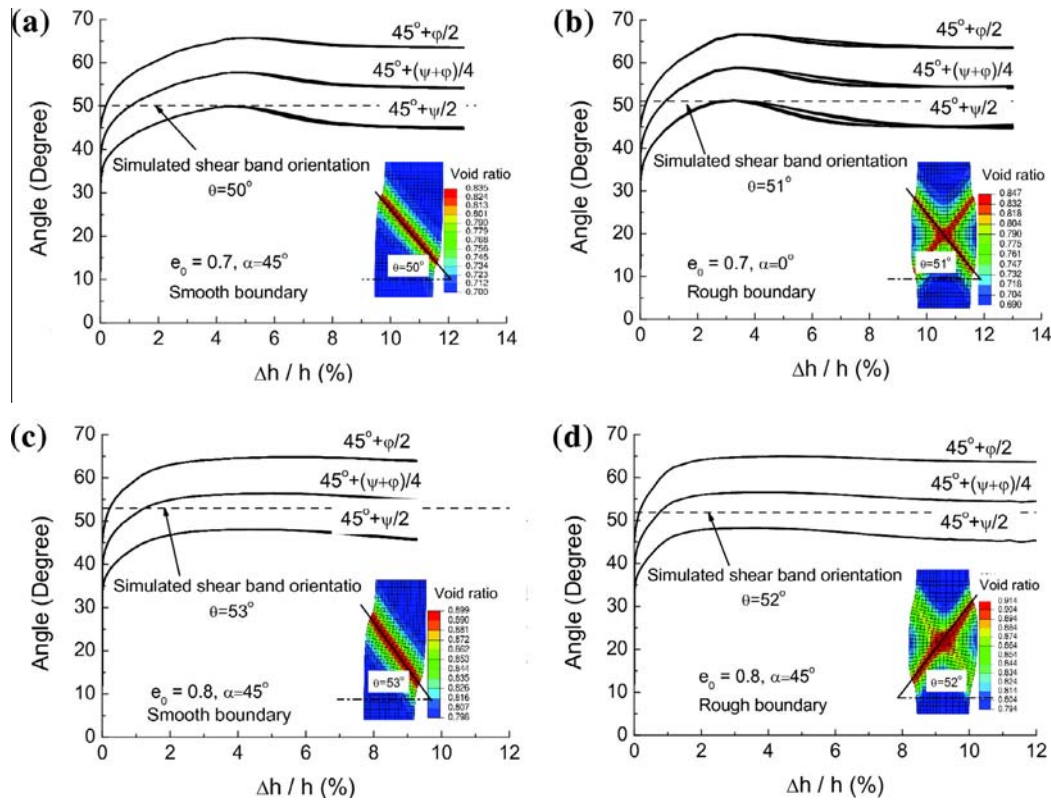


Fig. 23. Comparison between the simulated and theoretical shear band orientation for cases with (a) e₀ = 0.7, α = 45°, σ₃ = 400 kPa, smooth boundary (b) e₀ = 0.7, α = 0°, σ₃ = 400 kPa, rough boundary (c) e₀ = 0.8, α = 45°, σ₃ = 50 kPa, smooth boundary and (d) e₀ = 0.8, α = 45°, σ₃ = 50 kPa, rough boundary.

(ψ_{max} + φ_{max})/4, which is between the Roscoe's angle and Coulomb's angle. θ_A will be termed the Arthur's angle for convenience here. This relation was later derived by Vardoulakis (1980) based on the bifurcation theory. To obtain the values of the three theoretical angles, the evolution of the following three quantities (45° + ψ/2, 45° + φ/2 and 45° + (ψ + φ)/4) for all the four integration points of Element A inside the shear band as shown in Fig. 19 are monitored.

Fig. 23 shows a comparison between the simulated shear band orientations and the evolution of the theoretical angles for various initial and boundary conditions. In the figure, the values of ψ and φ at all four integration points of Element A during the entire loading process are calculated according to Eqs. (24) and (25) and are then used to obtain the three angles defined in Eqs. (21)–(23). So each case of shear band angle indeed includes four curves. Nevertheless, Fig. 23 shows that their values at all the four integration points of the element are very close or totally identical. The theoretical results are not affected by the exact location of the element as long as the element is not close to the vertical sides of the sample. The simulated final shear band angle is also measured from the deformed sample (see the inset of each figure) and its value is depicted by a dash line in Fig. 23. It can be seen that the simulated shear band orientation is the Roscoe's angle θ_R for cases with high confining pressure, independent of either the boundary condition or the bedding plane orientation (Fig. 23(a) and (b)), while it is in between θ_R and θ_A for the low confining pressure cases (Fig. 23(c) and (d)). While experimental observations show that the Coulomb's angle θ_C fits the shear band orientation better (Tatsuoka et al., 1990), the current simulations, being close to the Roscoe's angle, appear to underestimate this angle. The reason remains to be further investigated. A possible reason is that these theoretical values have been obtained for isotropic perfectly plastic media, while the present study considers an elasto-plastic anisotropic material. We note nevertheless that Tejchman and Górski (2010) and Gutierrez (2011) have also reported notable differences be-

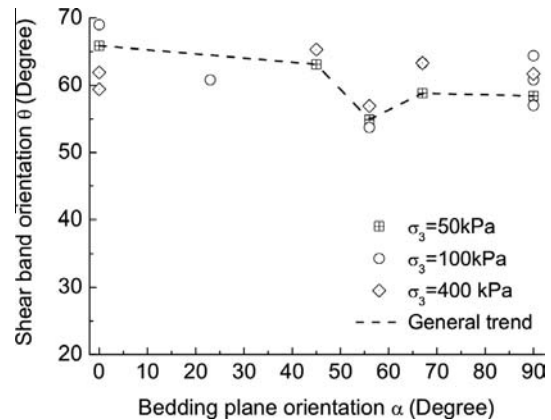


Fig. 24. Measured shear band orientation variation with the bedding plane orientation [data from Tatsuoka et al. (1990)].

tween numerically/analytically predicted and experimentally measured shear band angles. Moreover, since the measured peak friction angle varies with the initial bedding plane orientation, the experimental observed shear band orientation is not always a constant (see Fig. 24, data from Tatsuoka et al., 1990).

7. Conclusions

The effect of fabric and its evolution on strain localization in sand under plane strain compression has been investigated based on a newly developed anisotropic critical state model and FEM. The study realistically reproduces the behavior of strain localization in sand observed in laboratory tests by Tatsuoka et al. (1986) and Tatsuoka et al. (1990) and offers physically sounded

explanations on the different shear band patterns under different boundary conditions. The major observations and conclusions from this study are summarized as below.

- (a) The initiation of strain localization in a sand sample is a combined consequence of the structural constraint imposed by the boundaries and the pre-existing asymmetric soil fabric, with the former normally playing a major role.
- (b) Further development of shear band is governed by two mechanisms: the evolution of fabric and the structural constraint. Between the two, the structural constraint tends to exert more biased stress on the sample which leads to intensified strain localization on the existing shear band(s), while the fabric evolution may render the material response to be more coaxial with the applied load and hence help the sample to resist the external load more optimally to relieve strain localization. An explanation of the mechanisms has been provided for the shear band formation in smooth/rough boundary conditions.
- (c) In the case of smooth boundary condition, the applied load and boundary condition cause the initiation of strain localization at a very low strain level and dominates the subsequent deformation. The lately mobilized fabric evolution cannot change the well-established localized trend already developed in the sand sample. An asymmetric single shear band pattern (Type-b band) is observed in this case. Considering an evolving fabric or a constant fabric will not change the final observed pattern too much.
- (d) Rough boundary conditions lead to cross-shape double shear bands formed in the sand sample. If the fabric is free to evolve to accommodate the applied stress, the final shear bands become symmetric at large deformation. Otherwise, the first appearing Type-a shear band will dominate, which gives rise to an asymmetric cross-shape double-band pattern.
- (e) Significant volumetric expansion and fabric change can be observed inside the shear band, which is in agreement with the experimental observations (e.g., Oda et al., 1982). This is related to the bulking and reconstruction of the column-like structure in the sample.
- (f) The shear band angles obtained from our simulations are generally smaller than those observed in experimental tests. The predicted shear band angle in our study coincides with the Roscoe's angle for cases of high confining pressure and is in between the Roscoe's angle and the Arthur's angle for the low confining pressure case.

Since the main objective of this work is to investigate the effect of fabric and its evolution on strain localization in sand, uniform void ratio distribution, fixed sample dimension and loading mode (plane strain compression) have been used. In line with this work, future effort will be placed on aspects including the fabric effect on the other instability patterns such as diffuse failure (e.g., Daouadjji et al., 2011), shear band in sand under more general loading conditions (e.g., torsional shear and true triaxial tests) and the influence of random distribution of material properties and state variables in a sample. We note also that the current study has been carried out within conventional plasticity and cannot escape the famous mesh dependency issue in strain localization simulations. To overcome this, higher order or non-local continuum theories (e.g., Zhou et al., 2002; Zhao et al., 2005b, 2006, 2007; Zhao and Sheng, 2006) have to be further considered.

Acknowledgements

The study was financially supported by Research Grants Council of Hong Kong (through GRF 622910 and DAG08/09.EG04).

References

- Anand, L., Gu, C., 2000. Granular materials: constitutive equations and strain localization. *J. Mech. Phys. Solids* 48 (8), 1701–1733.
- Arthur, J.R.F., Dunstan, T., Al-Ani, Q.A.J.L., Assadi, A., 1977. Plastic deformation and failure in granular media. *Géotechnique* 27 (1), 53–74.
- Bardet, J.P., Proubet, J., 1991. A numerical investigation of the structure of persistent shear bands in granular media. *Géotechnique* 41 (4), 599–613.
- Bauer, E., Huang, W., Wu, W., 2004. Investigations of shear banding in an anisotropic hypoplastic material. *Int. J. Solids Struct.* 41, 5903–5919.
- Been, K., Jefferies, M.G., 1985. A state parameter for sands. *Géotechnique* 35 (2), 99–112.
- Chu, J., Lo, S.-C.R., Lee, I.K., 1996. Strain softening and shear band formation of sand in multi-axial testing. *Géotechnique* 46 (1), 63–82.
- Chupin, O., Rechenmacher, A.L., Abedi, S., 2011. Finite strain analysis of nonuniform deformation inside shear bands in sand. *Int. J. Numer. Anal. Methods Geomech.* 36 (14), 1651–1666.
- Dafalias, Y.F., Papadimitriou, A.G., Li, X.S., 2004. Sand plasticity model accounting for inherent fabric anisotropy. *J. Eng. Mech.* 130 (11), 1319–1333.
- Daouadjji, A., Darve, F., Al Gali, H., Hicher, P.Y., Laouafa, F., Lignon, S., Nicot, F., Nova, R., Pinheir, M., Prunier, F., Sibille, L., Wan, R., 2011. Diffuse failure in geomaterials: experiments, theory and modeling. *Int. J. Numer. Anal. Methods Geomech.* 35, 1731–1773.
- Desrues, J., Viggiani, G., 2004. Strain localization in sand: an overview of the experimental results obtained in Grenoble using stereophotogrammetry. *Int. J. Numer. Anal. Meth. Geomech.*, 279–321.
- Desrues, J., Chambon, R., Mokni, M., Mazerolle, F., 1996. Void ratio evolution inside shear bands in triaxial sand specimens studied by computed tomography. *Géotechnique* 46 (3), 529–546.
- Evans, T.M., Frost, J.D., 2010. Multiscale investigation of shear bands in sand: physical and numerical experiments. *Int. J. Numer. Anal. Methods Geomech.* 34, 1634–1650.
- Fu, P.-C., Dafalias, Y.F., 2011. Study of anisotropic shear strength of granular materials using DEM simulation. *Int. J. Numer. Anal. Methods Geomech.* 35, 1098–1126.
- Gao, Z.W., 2012. Constitutive modeling of anisotropic behavior in geomaterials: the role of fabric. PhD thesis, Hong Kong University of Science and Technology.
- Gao, Z.W., Zhao, J.D., Li, X.S., Dafalias, Y.F., 2013. A critical state sand plasticity model accounting for fabric evolution. *Int. J. Numer. Anal. Meth. Geomech.* in press. <<http://dx.doi.org/10.1002/nag.2211>>.
- Guo, N., Zhao, J.D., 2013. The signature of shear-induced anisotropy in granular media. *Comput. Geotech.* 47, 1–15.
- Gutierrez, M., 2011. Effects of constitutive parameters on strain localization in sands. *Int. J. Numer. Anal. Methods Geomech.* 35, 161–178.
- Hashiguchi, K., Tsutsumi, S., 2007. Gradient plasticity with the tangential-subloading surface model and the prediction of shear-band thickness of granular materials. *Int. J. Plast.* 23, 767–797.
- Hughes, T.J.R., Winget, J., 1980. Finite rotation effects in numerical integration of rate constitutive equations arising in large deformation analysis. *Int. J. Numer. Methods Eng.* 15, 1862–1867.
- Lade, P.V., 2003. Analysis and prediction of shear banding under 3D conditions in granular materials. *Soils Found.* 43 (4), 161–172.
- Lade, P.V., Nam, J., Hong, W.P., 2008. Shear banding and cross-anisotropic behavior observed in laboratory sand tests with stress rotation. *Can. Geotech. J.* 45, 74–84.
- Li, X.S., Dafalias, Y.F., 2000. Dilatancy for cohesionless soils. *Géotechnique* 50 (4), 449–460.
- Li, X.S., Dafalias, Y.F., 2004. A constitutive framework for anisotropic sand including non-proportional loading. *Géotechnique* 54 (1), 41–55.
- Li, X.S., Dafalias, Y.F., 2012. Anisotropic critical state theory: the role of fabric. *J. Eng. Mech.* 138 (3), 263–275.
- Li, X.S., Li, X., 2009. Micro–macro quantification of the internal structure of granular materials. *J. Eng. Mech.* 135 (7), 641–656.
- Li, X.S., Wang, Y., 1998. Linear representation of steady-state line for sand. *J. Geotech. Geoenviron. Eng.* 124 (12), 1215–1217.
- Mokni, M., Desrues, J., 1998. Strain localization measurements in undrained plane-strain biaxial tests on Hostun RF sand. *Mech. Cohes.-Fric. Mater.* 4, 419–441.
- Oda, M., Iwashita, K., 1999. *Mechanics of Granular Materials: An Introduction*. Taylor & Francis, Netherlands.
- Oda, M., Iwashita, K., 2000. Study on couple stress and shear band development in granular media based on numerical simulation analyses. *Int. J. Eng. Sci.* 38, 1713–1740.
- Oda, M., Kazama, H., 1998. Microstructure of shear bands and its relation to the mechanisms of dilatancy and failure of dense granular soils. *Géotechnique* 48, 465–481.
- Oda, M., Konishi, J., Nemat-Nasser, S., 1982. Experimental micromechanical evaluation of strength of granular materials: effect of particle rolling. *Mech. Mater.* 1 (4), 267–283.
- Rechenmacher, A.L., 2006. Grain-scale processes governing shear band initiation and evolution in sands. *Int. J. Solids Struct.* 54 (1), 22–45.
- Roscoe, K.H., 1970. The influence of strains in soil mechanics. *Géotechnique* 20 (2), 129–170.
- Shuttle, D.A., Smith, I.M., 1988. Numerical simulation of shear band formation in soils. *Int. J. Numer. Anal. Methods Geomech.* 12, 611–626.

- Sloan, S.W., 1987. Substepping schemes for the numerical integration of elastoplastic stress-strain relations. *Int. J. Numer. Methods Eng.* 24 (5), 893–911.
- Sloan, S.W., Abbo, A.J., Sheng, D.C., 2001. Refined explicit integration of elastoplastic models with automatic error control. *Eng. Comput.* 18, 121–154.
- Tatsuoka, F., Nakamura, S., Huang, C.C., Tani, K., 1990. Strength anisotropy and shear band direction in plane strain tests of sand. *Soils Found.* 30 (1), 35–54.
- Tatsuoka, F., Sakamoto, M., Kawamura, T., Fukushima, S., 1986. Strength and deformation characteristics of sand in plane strain compression at extremely low pressures. *Soils Found.* 26 (1), 65–84.
- Tejchman, J., Bauer, E., Wu, W., 2007. Effect of fabric anisotropy on shear localization in sand during plane strain compression. *Acta Mech.* 189, 23–51.
- Tejchman, J., Górski, J., 2010. Finite element study of patterns of shear zones in granular bodies during plane strain compression. *Acta Geotech.* 5, 95–112.
- Vardoulakis, I., 1980. Shear band inclination and shear modulus of sand in biaxial tests. *Int. J. Numer. Anal. Methods Geomech.* 4, 103–119.
- Vardoulakis, I., 1996. Deformation of water-saturated sand: I. Uniform undrained deformation and shear band. *Géotechnique* 46 (3), 441–456.
- Zhao, J.D., Sheng, D.C., 2006. Strain gradient plasticity by internal-variable approach with normality structure. *Int. J. Solids Struct.* 43 (18–19), 5836–5850.
- Zhao, J.D., Sheng, D.C., Collins, I.F., 2006. Thermomechanical formulations of strain gradient plasticity for geomaterials. *J. Mech. Solids Struct.* 1 (5), 837–863.
- Zhao, J.D., Sheng, D.C., Rouainia, M., Sloan, S.W., 2005a. Explicit stress integration of complex soil models. *Int. J. Numer. Anal. Methods Geomech.* 29, 1209–1229.
- Zhao, J.D., Sheng, D.C., Sloan, S.W., Krabbenhoft, K., 2007. Limit theorems for gradient-dependent elastoplastic geomaterials. *Int. J. Solids Struct.* 44 (2), 480–576.
- Zhao, J.D., Sheng, D.C., Zhou, W.Y., 2005b. Shear banding analysis of geomaterials by strain gradient enhanced damage model. *Int. J. Solids Struct.* 42 (20), 5335–5355.
- Zhao, J.D., Guo, N., 2013a. A new definition on critical state of granular media accounting for fabric anisotropy. *Powders and Grains 2013: AIP Conference Proceedings* 1542, 229–232. <<http://dx.doi.org/10.1063/1.4811909>>.
- Zhao, J.D., Guo, N., 2013b. Unique critical state characteristics in granular media considering fabric anisotropy. *Géotechnique* 63 (8), 695–704. <http://dx.doi.org/10.1680/geot.12.P.040>.
- Zhao, J.D., Guo, N., Li, X.S., 2013. Unique quantification of critical state in granular media considering fabric anisotropy. *Constitutive Modelling of Geomaterials: Springer Series in Geomechanics and Geoengineering*, 247–252. <http://dx.doi.org/10.1007/978-3-642-32814-5_31>.
- Zhou, W.Y., Zhao, J.D., Liu, Y.G., Yang, Q., 2002. Simulation of localization failure by strain-gradient-enhanced damage mechanics. *Int. J. Numer. Anal. Methods Geomech.* 26 (8), 793–813.